Taylor & Francis
Taylor & Francis Group

Characterization of novel pseudoelastic behaviour of zinc oxide nanowires

A. J. KULKARNI†, K. SARASAMAK‡,
S. LIMPIJUMNONG‡ and M. ZHOU*†

†The George W. Woodruff School of Mechanical Engineering, Georgia Institute
of Technology, Atlanta, Georgia 30332-0405, USA
‡School of Physics, Suranaree University of Technology and National
Synchrotron Research Center, Nakhon Ratchasima, Thailand

We recently reported the discovery of a novel pseudoelastic behaviour resulting from a reversible phase transformation from wurtzite ($P6_3mc$) to a novel graphite-like hexagonal ($P6_3/mmc$) structure in [01$\bar{1}$0]-oriented ZnO nanowires under uniaxial loading [Phys. Rev. Lett. **97** 105502 (2006)]. This previously unknown phenomenon is observed in nanowires and has not been reported for bulk ZnO. In this paper, molecular dynamics simulations are carried out to characterize the tensile behaviour dominated by this transformation of nanowires with lateral dimensions of 18–41 Å over the temperature range of 100–700 K. Significant size and temperature effects on the behaviour are observed. Specifically, the critical stress for the initiation of the phase transformation, the recoverable strains associated with the pseudoelasticity and the hysteretic energy dissipation are found to be both size and temperature dependent and can vary by as much as 59%, 32% and 57%, respectively. The large recoverable strains of 10–16% are unusual for the normally rather brittle ZnO ceramic and are due to both elastic stretch and the phase transformation in the slender one-dimensional nanowires. The hysteretic energy dissipation is in the range 0.05–0.14 GJ m^{-3} per cycle and such low levels are attributed to the relatively low energy barrier for the transformation. Unlike the pseudoelasticity in fcc metal nanowires of Cu, Ni and Au, which leads to a novel shape memory effect, the pseudoelasticity quantified here does not result in a shape memory of ZnO nanowires. The primary reason is the absence of an energy barrier for the phase transformation at zero stress.

1. Introduction

Pseudoelasticity and the shape memory effect (SME) are traditionally associated with shape memory alloys and elastomers [1]. Such effects have recently been discovered in single crystalline metal nanowires as a consequence of their nanoscale dimensionality [2–5]. We have recently reported a novel pseudoelastic behaviour in [01$\bar{1}$0]-oriented ZnO nanowires which arises from a reversible phase transformation from a tetrahedrally coordinated wurtzite (herein denoted as WZ, $P6_3mc$ space group) phase to a newly discovered graphite-like phase (herein denoted as HX,

---

$P6_3/mmc$ space group) [6]. This previously unknown five-fold coordinated polymorph of ZnO can result from either tensile loading along the $[01\bar{1}0]$ direction or compressive loading along the [0001] direction. For $[01\bar{1}0]$ nanowires in tension, recoverable strains, which comprise of the elastic stretching of the WZ and HX phases and a contribution from the transformation, can be up to 16%. This is quite extraordinary since ionic compound semiconductors such as ZnO, GaN, InN and BN are known to be brittle under tensile loading. While the ability to undergo a phase transformation is the primary reason for the unusual pseudoelastic behaviour, the nearly defect-free nature of these nanowires and the large surface-to-volume ratios, which enhance atomic mobility, also contribute to the wires' ability to undergo deformation without fracture. The high strengths, large recoverable strains and property variations associated with transformation make these nanowires ideal candidates for nanocomponents in a variety of nano-electromechanical systems (NEMS), such as sensors, actuators and switches. Since this pseudoelastic behaviour has just been discovered in ZnO nanowires that have only been synthesized recently, a fundamental understanding of the overall constitutive behaviour, the nature of the phase transformation and the characteristics of the transformed phase is needed in order to unleash the potential of these nanowires.

In this paper, the pseudoelastic responses of $[01\bar{1}0]$ ZnO nanowires with lateral dimensions of 21.22×18.95, 31.02×29.42 and $40.81 \times 39.89\,\text{Å}^2$ under quasistatic tensile loading are characterized. The characterization accounts for temperatures between 100 and 700 K. The analysis focuses on the formation of the new HX crystalline structure and the transformation path from WZ to HX under uniaxial tensile loading. In particular, the atomic motions or lattice distortion resulting in the formation of the HX structure are quantified through the gradient of a continuum deformation map. The analysis lends itself to the quantification of the recoverable strains associated with the pseudoelastic behaviour of the nanowires, including contributions from the elastic stretching of the WZ and the HX phases and lattice size change due to the phase transformation. The size and temperature dependence of important parameters, including the critical stress for the initiation of phase transformation, maximum recoverable strain and hysteretic dissipation, are also quantified.

2. Computational framework

Molecular dynamics (MD) simulations using the Buckingham potential with charge interactions [7, 8] are carried out. The nanowires considered are single-crystalline and wurtzite-structured, with lattice constants $a = 3.249\,\text{Å}$ and $c = 5.206\,\text{Å}$ and a growth direction along the $[01\bar{1}0]$ axis [9–11]. The wire structure is generated by repeating a wurtzite unit cell along the $[2\bar{1}\bar{1}0]$, [0001] and $[01\bar{1}0]$ directions (figure 1). Three different cross-sectional sizes (21.22×18.95, 31.02×29.42 and $40.81 \times 39.89\,\text{Å}^2$) are considered. The smallest cross-sectional size ($21.22 \times 18.95\,\text{Å}^2$) is chosen such that the short-range cut-off distance in the Buckingham potential [7, 8] is smaller than the smallest wire dimension and long-range interactions are properly considered [12]. Periodic boundary conditions are specified in the axial direction. Calculations with
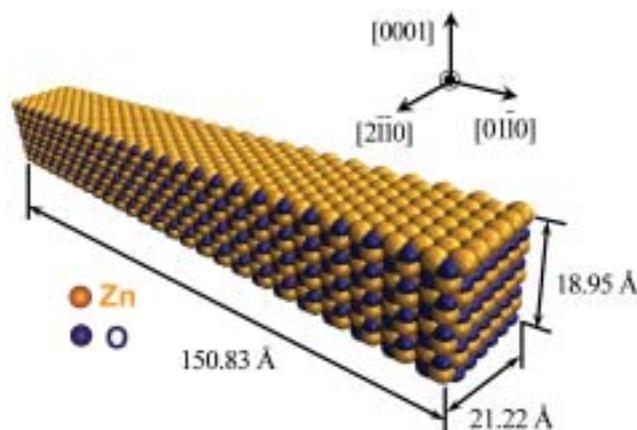
Figure 1. Configuration of a [01$\bar{1}$0] nanowire with lateral dimensions of $21.22 \times 18.95 \text{Å}^2$ after geometric construction and before initial relaxation.

different computational cell sizes show that any length greater than 100 Å, irrespective of the cross-section size, is sufficient to avoid image effects [13, 14]. Here, a periodic computational cell length of 150.83 Å is used for all the cross-sections analyzed.

Since the crystallographically constructed nanowires may not be in equilibrium, preloading relaxations are carried out to obtain the wires' free-standing configurations. The relaxations occur at desired temperatures without external loading, until thermodynamic quantities (such as energy, stress, and temperature) indicate that statistical steady states have been reached. A relaxation time of 3 ps is found to be adequate for achieving equilibrium states for the ranges of wire size and temperature considered. During the relaxations, minimization of the wires' energy occurs through surface reconstruction and adjustment of the lattice spacing in the wire core. The surface reconstruction manifests in the forms of decreases in the interlayer spacing between outer surface layers and in-plane contractions of the surfaces [13]. Such morphological changes on surfaces and in the wires' cores are also monitored. This is especially important for nanostructures since their surface-to-volume ratios are high and extensive surface, and in some cases, core reconstructions may occur. For example, [100] oriented fcc metal nanowires are known to reconstruct into [110] orientations as a consequence of surface energy minimization [2, 4, 15, 16].

Following the initial relaxations, a quasistatic loading scheme is employed to effect tensile deformation and to obtain the mechanical response of the nanowires. Approximate quasistatic tensile loading in each deformation increment is achieved though successive loading and equilibration steps using a combination of algorithms for NPT and NVE ensembles [17]. Specifically in each deformation increment, stretching at a specified rate of 0.005 ps^{-1} is first carried out for 0.5 ps using a modified version of the NPT algorithm of Melchionna *et al.* [18, 19]. Subsequently, with the strain maintained constant, the nanowire is relaxed for 3 ps via an algorithm for NVE ensemble [17] at the specified temperature. This equilibration duration is chosen such that a statistically steady state is reached and no further structural
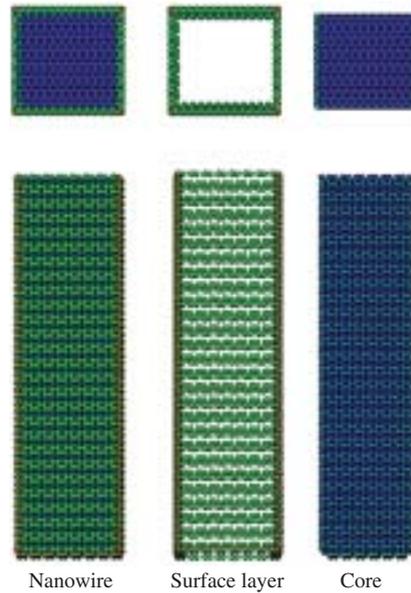
A. J. Kulkarni et al.

Figure 2.   Decomposition of a nanowire into surface atoms and interior atoms using the
coordination number (CN); the surface atoms have CNs below 4 and the core atoms have CNs
equal to 4.

changes occur. It is possible that the magnitude of the strain increment in each step
may affect the calculated stress-strain response. To minimize this error, calculations
using series of strain increments between 0.35% and 0.1% were carried out. Based on
the results, a strain increment of 0.25% and an equilibration period of 3 ps per
loading step are found to minimize fluctuations in the calculated response and are
used in the analysis reported. Since the loading proceeds in a series of equilibration
steps, this process essentially simulates quasistatic loading of the specimen.
Unloading is implemented in a similar manner with a reduction in strain for each
unloading step. The virial formula is used to calculate the stress [20].

Changes in lattice structures are characterized using the average lattice constants
and the radial distribution function (RDF) [21]. The average lattice constants are
calculated at each strain increment by averaging local lattice constants over the bulk
volume of the wire. Surface layers (figure 2) are not included in this calculation and
the local lattice parameters are computed from coordinates of atoms in the wire core.
The RDF describes how atoms in a system are radially packed around each other.
It measures the density of atoms in a spherical shell of radius r and thickness dr
surrounding an atom in the structure, i.e.

$$g(r) = \frac{n(r,\,r+dr)/V_S}{N/V}, \tag{1}$$

where $g(r)$ is the RDF, $n(r, r+dr)$ is the number of atoms in the spherical shell,
$V_S = 4\pi r^2 dr$ is the volume of the spherical shell, N is the total number of atoms in the
system and V is the volume of the structure. The RDFs are generated at the end

of the equilibration stage of a relevant strain increment when a steady state has been achieved. In particular, the RDFs for the WZ structure after initial relaxation and for the HX structure after transformation completion are studied to characterize the structural changes associated with the phase transformation.

3. Results and discussion

3.1. *Loading response*

Figure 3a shows the tensile stress–strain curve of a $40.81 \times 39.89 \, \text{Å}^2$ wire during loading and unloading at 100 K. The configurations of this wire at four different stages (three of which are during loading) of deformation along the curve are shown in figure 3b, with the atoms coloured by their coordination numbers. In the wurtzite structure [initial configuration, (i) in figure 3b], each atom has a coordination number of 4, typical for tetrahedral structures. Atoms on surfaces and edges have coordination numbers of 3 or less. In the HX phase [(ii) and (iii) in figure 3b], on the other hand, each atom has a coordination number of 5 due to an additional Zn–O bond along the [0001] axis as compared to the WZ phase. This five-fold coordination will be discussed later.

The loading response (figure 3a) consists of initial elastic stretching of the WZ wire (A → B), structural transformation from WZ to HX (B → D) and elastic stretching of the HX wire (D → E), culminating in the eventual failure at E. The stress–strain relation in the elastic regime between A and B is essentially linear. Deformation beyond the elastic regime results in a stress drop from 11.31 to 10.45 GPa (B → C). This relaxation event indicates the initiation of a phase transformation [22]. The HX phase nucleates near the wire's surface at a strain of 0.065 (figure 3a). As the deformation progresses, the transformed region sweeps through the whole specimen [C → D and configuration (ii) in figure 3b] and the transformation is completed at a strain of 0.108 and a stress of 10.58 GPa (point D in figure 3a). Continued loading beyond point D causes elastic stretching of the transformed structure [D → E in figure 3a and configuration (iii) in figure 3b] and the eventual failure at a strain of 0.162 and a stress of 12.28 GPa through cleavage along $(\bar{1}2\bar{1}0)$ type planes.

3.2. *Crystallographic change*

Figure 4 outlines the crystallographic characteristics of the initial WZ phase and the transformed HX phase. Following Limpijumnong and co-workers [23, 24], a common set of lattice parameters (a, b, c, uc and vb) for these two structures is used and illustrated in figure 4a. Additionally, two layers of atoms perpendicular to the [01$\bar{1}$0] direction and two layers perpendicular to the [2$\bar{1}\bar{1}$0] direction are shown in figures 4b and c, respectively, to delineate the atomic motions associated with the transformation. The figure shows that, as a result of the transformation, the (0001) Zn and O basal planes become coplanar and the HX structure acquires a new symmetry (mirror plane perpendicular to the [0001] axis). Consequently, an
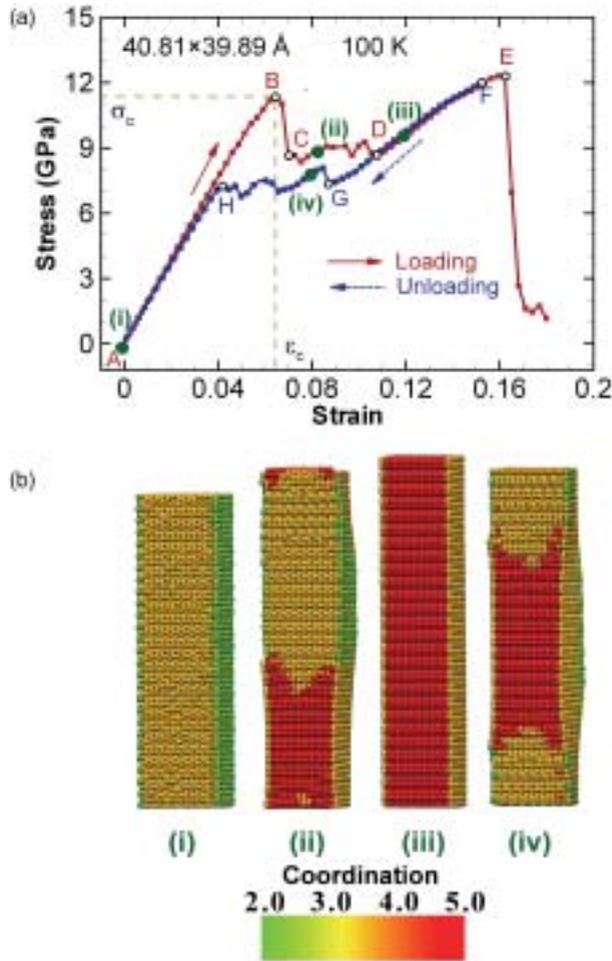
Figure 3. Tensile behaviour of a $40.81 \times 39.89\,\text{Å}^2$ nanowire: (a) stress–strain curve under loading and unloading; (b) deformed configurations at different stages of loading and unloading.

additional Zn–O bond is formed along the [0001] axis (figures 4b and c), giving the HX phase a five-fold coordination. Table 1 lists the lattice parameters for the WZ and HX structures at several stress levels for the $40.81 \times 39.89\,\text{Å}^2$ wire. During the deformation, $u = uc/c$ changes from its initial value of 0.4 for WZ to a value of 0.5 for HX, implying the flattening of buckled wurtzite basal planes. A similar unbuckled structure has been observed in GaN, MgO and ZnO thin films as a result of extensive surface reconstructions to suppress surface polarity [25–28].

Figure 5 shows the RDF profiles before loading is applied (point A, $\sigma = 0\,\text{GPa}$) and upon completion of the WZ → HX transformation (point D, $\sigma = 8.58\,\text{GPa}$) for the nanowire in figure 3. The profile for the initial wire (WZ structure) has its first
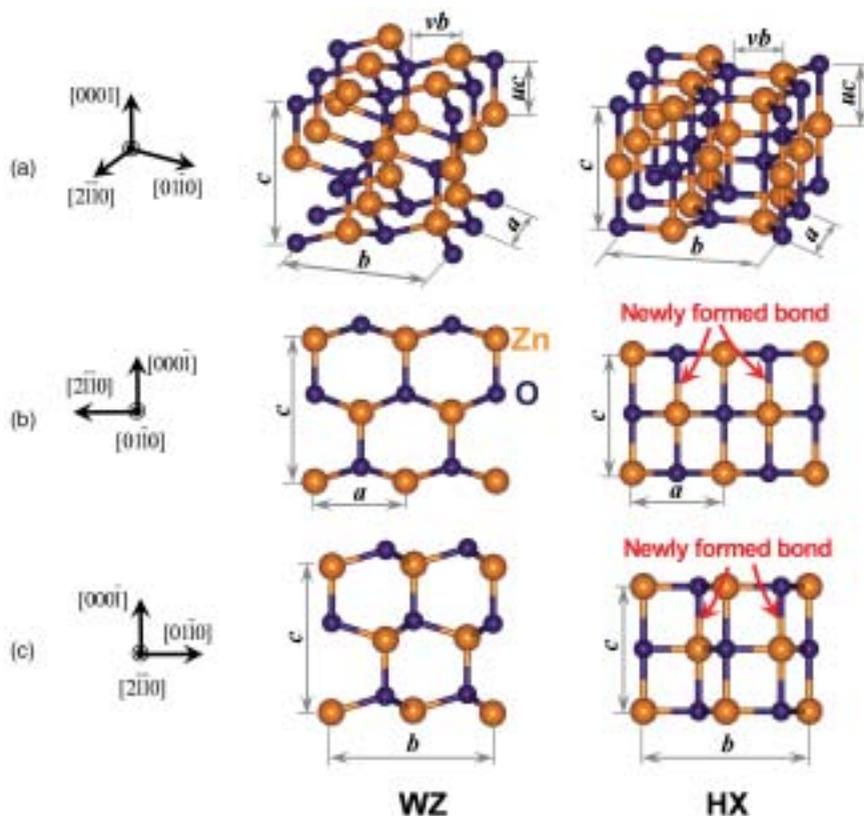
Figure 4. Illustrations of the WZ and HX structures involved in the phase transformation: (a) lattice structures of the WZ and HX phases; (b) atomic arrangement on [01$\bar{1}$0] plane; (c) atomic arrangement on [2$\bar{1}$$\bar{1}$0] plane.

Table 1. Lattice parameters for WZ, HX and RS under different loading conditions for a $40.81 \times 39.89 \, \text{Å}^2$ nanowire.

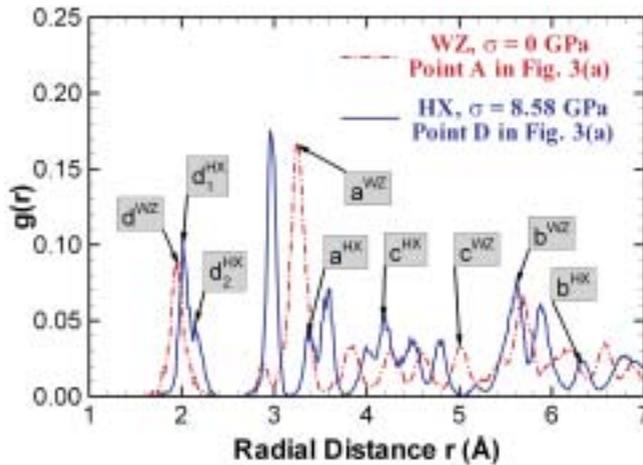| Parameter	WZ			HX	
	$\sigma = 0 \, \text{GPa}$ $\varepsilon = 0^a$	$\sigma = 0 \, \text{GPa}$ $\varepsilon = 0$	$\sigma = 11.39 \, \text{GPa}$ $\varepsilon = 0.065$	$\sigma = 8.58 \, \text{GPa}$ $\varepsilon = 0.108$	$\sigma = 12.29 \, \text{GPa}$ $\varepsilon = 0.162$
(Å)	3.25	3.26	3.23	3.38	3.40
b (Å)	5.63	5.62	6.05	6.22	6.62
v	0.33	0.32	0.29	0.31	0.29
c (Å)	5.21	5.18	4.92	4.30	4.15
u	0.38	0.41	0.46	0.50	0.49
b/a	1.73	1.74	1.87	1.84	1.95
c/a	1.60	1.57	1.53	1.27	1.22

[a]Experiment [29].

Figure 5. Radial distribution function profiles for a $40.81 \times 39.89 \, \text{Å}^2$ nanowire before loading (point A in figure 3a] and upon completion of phase transformation (point D in figure 3a).

peak at a radial distance of 1.93 Å, indicating a Zn–O bond distance consistent with the experimental value of 1.95 Å [29]. Upon completion of the WZ $\rightarrow$ HX transformation at point D, this peak has split into two peaks with the primary peak at 1.98 Å and the secondary peak at 2.20 Å. The primary peak corresponds to Zn–O bonds in the basal ({0001}) plane of the HX structure, while the secondary peak is associated with the additional bonds formed along the [0001] axis (see figure 4). Also seen in figure 5 are peaks corresponding to lattice constants a, b and c. Initially in the WZ phase, the 'a' peak is at 3.26 Å and the 'c' peak is at 5.18 Å. The transformation to HX results in the shift of the 'a' peak to 3.38 Å and the shift of the 'c' peak to 4.30 Å. These shifts indicate that the transformation to the HX structure involves both an expansion of the basal planes (increase in 'a') to accommodate the flattening of the buckled plane and a contraction in 'c' which results in the formation of the Zn–O bond along the [0001] axis. The transformation is also associated with a shift of the 'b' peak from 5.60 Å for WZ to 6.22 Å for HX, consistent with the nature of the applied tensile loading. The values reported in table 1 also show a progressive increase in the lattice parameter b toward 6.22 Å as the stress is increased towards the level of 8.58 GPa at the completion of the transformation. Further load increases are accompanied by increases in b with the associated RDF peak shifting toward a higher value (not shown).

3.3. *Characterization of the deformation*

The deformation can be quantified in a continuum sense through the deformation gradients F_i ($i = 1, 2$, and 3) associated with the three stages of deformation, with $i = 1$ denoting the first stage (elastic stretching of WZ, A $\rightarrow$ B in figure 3a), $i = 2$ denoting the second stage (transformation from WZ to HX, B $\rightarrow$ D in figure 3a) and $i = 3$ denoting the third stage (elastic stretching of HX, D $\rightarrow$ E in figure 3a). In such
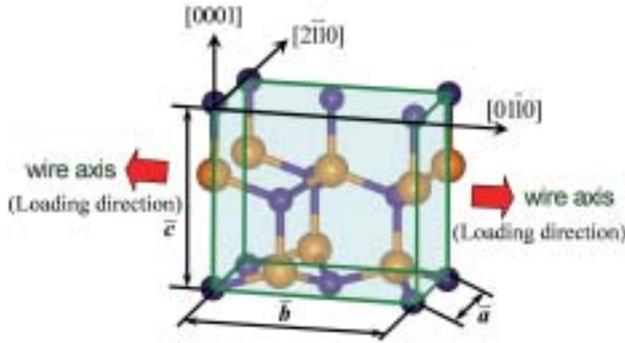
Figure 6. Representative volume defined in a unit cell of the wurtzite lattice for the purpose of deformation analysis.

an analysis, the deformation of a representative volume of $\Omega = \bar{a} \times \bar{b} \times \bar{c}$ (figure 6) is used, with dimensions $\bar{a}$, $\bar{b}$ and $\bar{c}$ being the average values of lattice constants a, b and c, respectively. Since the average values of the lattice parameters are used here, the deformed wire is regarded as a repetition of this representative volume. The deformation gradient for each stage can then be expressed as

$$
\boldsymbol{F}_i = \begin{pmatrix} \dfrac{\bar{a}_i}{\bar{a}_{i-1}} & 0 & 0 \\ 0 & \dfrac{\bar{c}_i}{\bar{c}_{i-1}} & 0 \\ 0 & 0 & \dfrac{\bar{b}_i}{\bar{b}_{i-1}} \end{pmatrix}, \quad i = 1, 2, 3. \tag{2}
$$

In the above expressions, $\bar{a}_{i-1}$, $\bar{b}_{i-1}$, and $\bar{c}_{i-1}$ are the average lattice constants at the beginning of stage i and $\bar{a}_i$, $\bar{b}_i$, and $\bar{c}_i$ are the average lattice constants at the end of stage i. Note that $\bar{a}_0$, $\bar{b}_0$, and $\bar{c}_0$ are the constants for the initial (undeformed, WZ) wire. The relative volume change associated with stage i is

$$
\frac{\Omega_i}{\Omega_{i-1}} = \det(\boldsymbol{F}_i), \tag{3}
$$

where Ω is the volume of the wire at the beginning and end of stage i, respectively.

For a $40.81 \times 39.89\,\text{Å}^2$ wire at 100 K, the deformation gradient for the first stage ($A \rightarrow B$ in figure 3a) is

$$
\boldsymbol{F}_1 = \begin{pmatrix} 0.991 & 0 & 0 \\ 0 & 0.960 & 0 \\ 0 & 0 & 1.065 \end{pmatrix}. \tag{4}
$$

The associated volume increase is 1.27% and the longitudinal (elastic) strain $\varepsilon_{33} = F_1^{33} - 1 = 0.065$ consistent with that seen from the stress-strain curve in figure 3.

During the second stage of deformation (phase transformation $B \rightarrow D$ in figure 3a), $\bar{a}$ increases and $\bar{c}$ decreases. The corresponding deformation gradient is

$$F_2 = \begin{pmatrix} 1.047 & 0 & 0 \\ 0 & 0.876 & 0 \\ 0 & 0 & 1.043 \end{pmatrix}. \tag{5}$$

The volume ratio associated with the transformation is $\Omega_2/\Omega_1 = 0.957$, indicating a slight decrease in volume of 4.3%. This decrease in volume under tensile loading is counterintuitive. It is a direct consequence of the discrete lattice structure and the structural transformation. Specifically, the uniaxial tensile stress in the [01$\bar{1}$0] or 'b' direction causes the interatomic distances in the [0001] Zn and O basal planes (a) to increase, causing the two types of basal planes to become coplanar and, therefore, the volume decrease.

The deformation gradient for the elastic deformation of the HX phase in the third stage ($D \rightarrow E$ in figure 3a) is

$$F_3 = \begin{pmatrix} 1.008 & 0 & 0 \\ 0 & 0.962 & 0 \\ 0 & 0 & 1.05 \end{pmatrix}. \tag{6}$$

Although the 'a' and 'b' directions are perpendicular to each other, a increases slightly (with a corresponding strain of $\varepsilon_{11} = 0.008$) under the tensile loading along the 'b' direction. This gives rise to a negative phenomenological Poisson's ratio of

$$\nu_{13} = -\frac{\varepsilon_{11}}{\varepsilon_{33}} = -0.16. \tag{7}$$

The total elastic strain of the wire beyond the completion of the phase transformation and before fracture (between D and F in figure 3a) is $\varepsilon_{33} = F_3^{33} - 1 = 0.05$. Here, the reference state of this strain is the length of the wire at the completion of transformation (point D). The corresponding volume increase is 1.68%.

Overall, the total strain of the wire between points A and E is $\varepsilon = F_1^{33} F_2^{33} F_3^{33} - 1 = 0.162$. Here, the reference length is the original length of the wire.

3.4. *Unloading response*

Unloading of an HX structured wire from any strain prior to wire fracture activates a novel pseudoelastic behaviour. Take the wire in figure 3 for example; unloading from a strain of 14.5% (point F) initially results in the recovery of the elastic straining of the HX structure embodied in F_3 and goes beyond the end point of the WZ $\rightarrow$ HX transformation during loading (point D). This elastic unloading within the HX structure continues until point G where a reverse transformation from HX to WZ initiates at a strain of 0.087 and a stress of 7.38 GPa. Further unloading results in the complete reversal of the HX $\rightarrow$ WZ transformation at H (with a strain of 0.039 and a stress of 7.04 GPa). Unloading between H and A follows the elastic trend of the WZ phase and the hysteresis loop is completed.

For the wire in figure 3, the total recoverable strain is $\sim$16% which is significant since ZnO is a ceramic. The hysteretic energy dissipation in one loading and

unloading cycle is $\sim 0.14\,\mathrm{GJ\,m^{-3}}$. This dissipation level is significantly lower than that observed for wurtzite to rock salt ($\mathrm{WZ} \rightarrow \mathrm{RS}$) transformations in bulk ZnO ($\sim 1.38\,\mathrm{GJ\,m^{-3}}$ per cycle), therefore, limiting heat generation and heat-related damage and making the nanowires ideal for applications involving cyclic loading and unloading [30]. The low level of dissipation can be attributed to the fact that (i) the crystallographic transition between the WZ and HX structures, which does not require the formation of defects such as dislocations or twin boundaries, is smooth and (ii) the energy barrier for the transformation between the WZ and the HX structures is relatively low [6].

3.5. *Effects of size and temperature*

Temperature and lateral dimensions have significant effects on the pseudoelastic behaviour of the wires. Figures 7a–c show the loading part of the stress–strain curves over 100–700 K for the 21.22×18.95, 31.02×29.42 and $40.81 \times 39.89\,\text{Å}^2$ nanowires, respectively. The critical stress for the nucleation of the HX phase (σ_c) is marked by open circles in these figures. Figure 7d shows the variation of this critical stress as a function of size and temperature. Overall, the critical stress decreases as the wire size
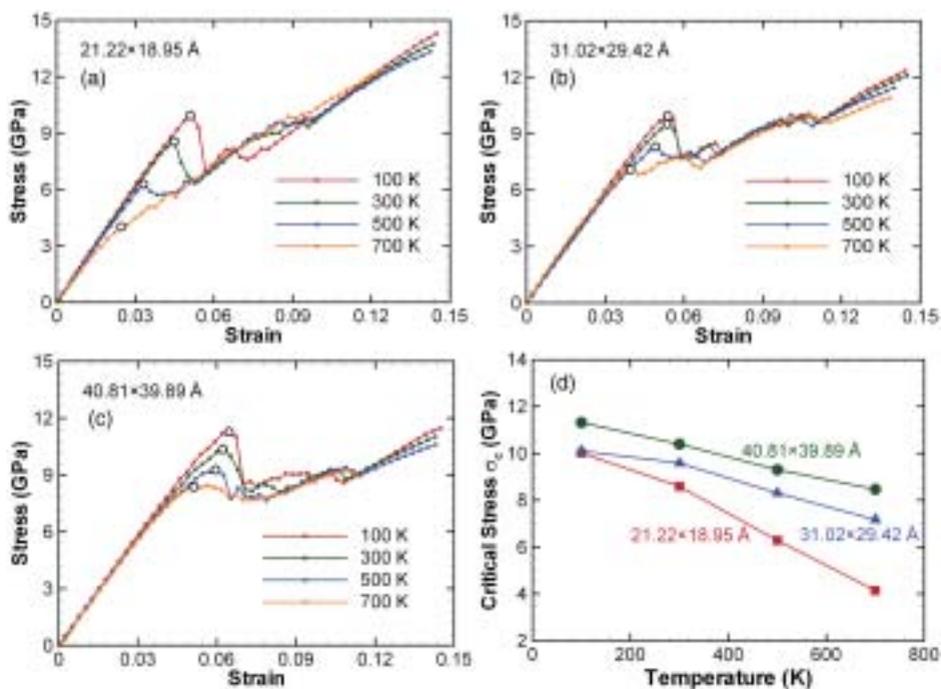

Figure 7. Stress–strain curves of (a) a $21.22 \times 18.95\,\text{Å}^2$ wire, (b) a $31.02 \times 29.42\,\text{Å}^2$ wire and (c) a $40.81 \times 39.89\,\text{Å}^2$ wire at different temperatures. (d) The critical stress for the initiation of phase transform (σ_c) as a function of lateral dimensions and temperature.
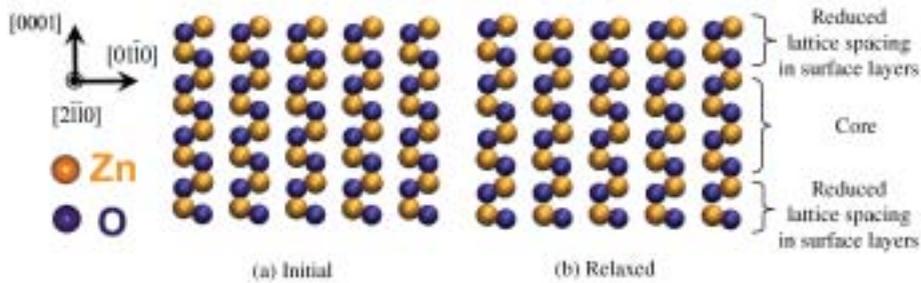
Figure 8.   Surface reconstruction of a $21.22 \times 18.95\,\text{Å}^2$ nanowire at $100\,\text{K}$ relative to its configuration in bulk ZnO, the images correspond to the states of the wire after (a) geometric construction (before initial relaxation) and (b) after initial relaxation.

is reduced. The critical stress also decreases as temperature is increased. Over the temperature range analyzed, σ_c for the $31.02 \times 29.42\,\text{Å}^2$ wire is up to 42% higher than that for the $21.22 \times 18.95\,\text{Å}^2$ wire, whereas the values for the $40.81 \times 39.89\,\text{Å}^2$ wire are approximately 11–15% higher than those for the $31.02 \times 29.42\,\text{Å}^2$ wire. In contrast to the well-established trend that the stiffness of nanowires increases as wire size is reduced [13], σ_c decreases as the wire size is reduced. The higher surface-to-volume ratios at smaller wire sizes cause both effects. Note that, as the wire size is reduced from $50\,\text{Å}$ to $10\,\text{Å}$, the surface-to-volume ratio increases by $\sim$35%. In particular, for polar (0001) surfaces (figure 1), the imbalance of charges results in extensive surface reconstruction.

Figure 8 shows the positions of atoms on layers perpendicular to the [0001] direction before and after the initial relaxation. Obviously, relative to the ideal bulk structure, the surface layers contract and the Zn and O basal planes become essentially coplanar, resulting in a layered surface structure (LY) which is crystallographically similar to the HX structure. This phenomenon has been predicted by first-principle calculations and observed in experiments on ZnO nanofilms [25, 26]. The reconstructed LY surfaces in the initial wire before loading play an important role because they can act as nucleation sites for and lower the energy barrier of the WZ $\rightarrow$ HX transformation due to the geometric similarities between the LY and HX structures. The smaller wire cores at smaller wire sizes facilitate the initiation of the phase transformation from the surfaces, resulting in the lower σ_c values.

As the temperature increases from $100\,\text{K}$ to $700\,\text{K}$, a 25.2% decrease in σ_c is observed for the $40.81 \times 39.89\,\text{Å}^2$ wire (figure 7d). This effect is attributed to thermal softening and the ability of the nanowire to overcome the energy barrier for the transformation at higher temperatures. Note that over the same range of temperature, the elastic modulus of the nanowire decreases by 24% [13]. Temperature changes also significantly affect hysteretic dissipation. To illustrate this effect, the stress-strain curves of the $40.81 \times 39.89\,\text{Å}^2$ wire at $100\,\text{K}$, $300\,\text{K}$, $500\,\text{K}$ and $700\,\text{K}$ are shown in figure 9.

The corresponding dissipation during the loading–unloading cycle, along with those for the 21.22×18.95 and $31.02 \times 29.42\,\text{Å}^2$ wires at these temperatures, is given
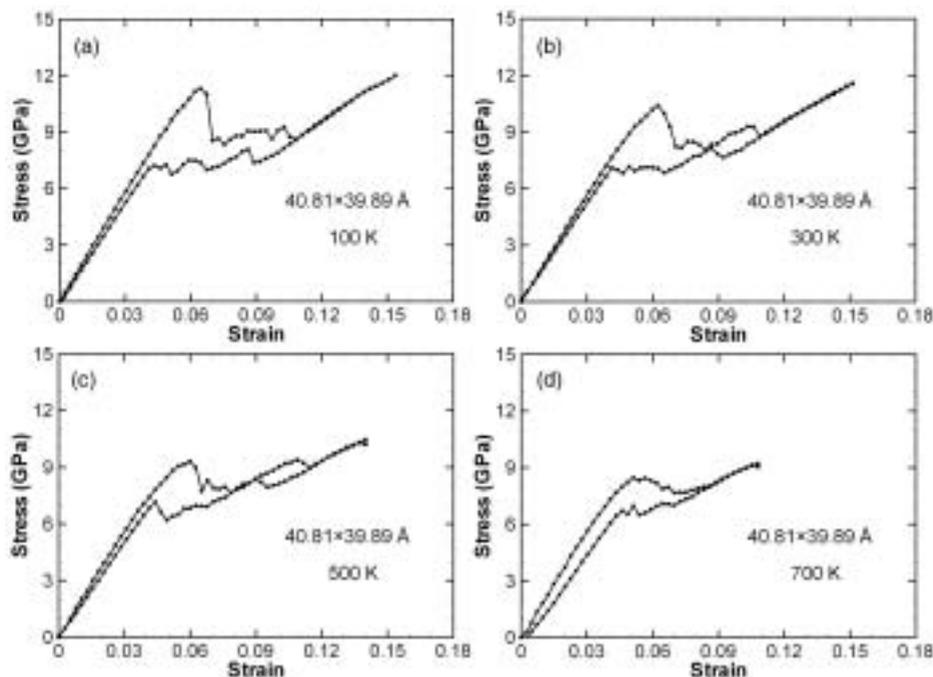
Figure 9. Stress–strain responses of a $40.81 \times 39.89 \, \text{Å}^2$ wire during one loading–unloading cycle at (a) 100 K, (b) 300 K, (c) 500 K and (d) 700 K.
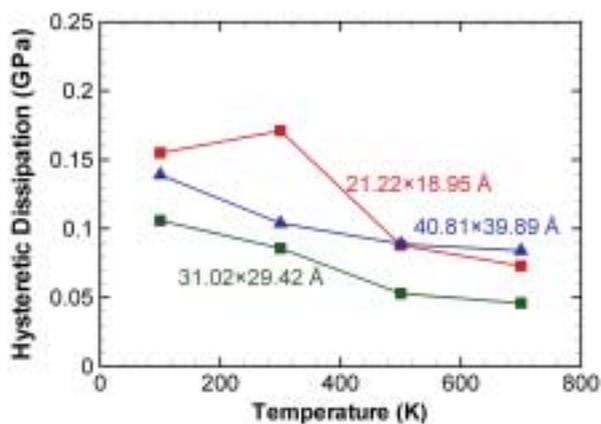

Figure 10. Hysteretic dissipation in one loading–unloading cycle as a function of lateral dimensions and temperature.

in figure 10. For the $40.81 \times 39.89 \, \text{Å}^2$ wire, the dissipation decreases by 39.6% as temperature is increased from 100 K to 700 K. A similar trend is seen for the 21.22×18.95 and $31.02 \times 29.42 \, \text{Å}^2$ wires which show decreases of 52.9% and 56.6%, respectively, over the same temperature range.

Table 2. Size and temperature dependence of the stress–strain response of the nanowires.

Cross-section dimensions (Å^2)	Temperature (K)	σ_c (GPa)	ε_c	Strain at completion of transformation	Maximum recoverable strain	Ultimate tensile strength (GPa)	Hysteretic dissipation (GJ m^{-3})
21.22×18.95	100	10.02	0.051	0.100	0.165	15.56	0.155
	300	8.59	0.045	0.096	0.155	14.50	0.171
	500	6.29	0.033	0.097	0.148	13.56	0.088
	700	4.15	0.027	0.091	0.127	12.34	0.073
31.02×29.42	100	10.10	0.053	0.110	0.155	13.05	0.106
	300	9.59	0.053	0.110	0.154	12.50	0.086
	500	8.31	0.049	0.098	0.140	11.44	0.053
	700	7.17	0.040	0.116	0.138	10.89	0.046
40.81×39.89	100	11.32	0.065	0.108	0.159	12.30	0.139
	300	10.40	0.063	0.109	0.162	11.68	0.104
	500	9.31	0.060	0.114	0.143	10.60	0.089
	700	8.47	0.051	0.086	0.108	9.21	0.084

Table 2 lists the values of several key parameters quantifying the pseudoelastic behaviour at various cross-sectional sizes and temperatures. In particular, note that the maximum recoverable strain decreases significantly as temperature is increased, while the strain at which the $WZ \rightarrow HX$ transformation completes is essentially temperature-independent. The enhanced mobility of atoms at higher temperatures promotes the formation of defects and may be a factor contributing to the failure at lower strain levels.

3.6. *Pseudoelasticity without shape memory*

The pseudoelastic behaviour quantified here is reminiscent of a very similar pseudoelastic behaviour (which leads to a novel shape memory effect) in fcc metal nanowires discovered and analyzed by Liang *et al.* [3, 4]. This similarity in the pseudoelastic behaviours between nanowires of the two classes of materials naturally raises the question of whether a similar SME also exists in the ZnO nanowires analyzed here. To answer this question, we first note that the pseudoelasticity and the SME in the fcc metal nanowires are driven primarily by a surface-stress-induced lattice reorientation process which requires the formation of intermediate transitional structures involving partial dislocations. One attribute of that unique lattice reorientation process is that an energy barrier exists between the phases even at very low temperatures. Therefore, spontaneous relaxation occurs only at temperatures above a critical value. It is this temperature dependence that gives rise to the SME in the fcc metal wires.

To ascertain if a SME exists in the ZnO nanowires analyzed here, partially and fully transformed wires were cooled to various final temperatures, the lowest being 10 K. Subsequently, unloading is carried out at the low temperatures to determine if the HX phase can be retained without external stress. For all wire sizes considered and under all initial/final temperature combinations analyzed, the wires reverted
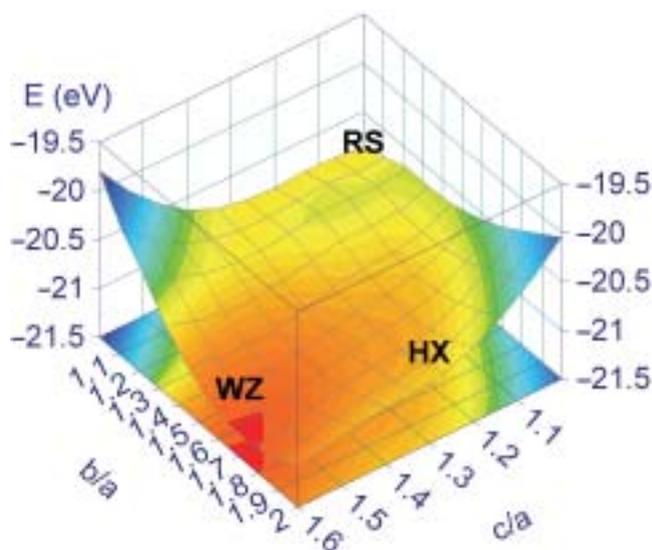
Figure 11. Potential energy map of ZnO with highlights of the WZ, RS and HX lattice structures.

fully back to the WZ structure. This result shows that there is no critical temperature below which either partially or fully HX-structured wires can exist without external loading. The absence of such a critical temperature and the lack of an HX structure at zero loading effectively rule out the possibility of a SME in the ZnO nanowires. This finding can be explained by the enthalpy surface for ZnO at 0 K and zero external loading. Figure 11 shows the potential energy profile of one ZnO unit cell at different structural configurations (when there is no external loading, the enthalpy is equal to the potential energy). This profile is obtained through first principle calculations, details of which are provided by Kulkarni *et al.* [6] and Limpijumnong and Jungthawan [23]. Lattice structures corresponding to WZ, RS and HX are labelled in this figure. Note that only two local minima (energy wells) exist, one at the WZ structure and the other at the RS structure. A well is not seen at the HX structure. Obviously, WZ is the stable phase and any sample with the HX structure would spontaneously transform into the WZ structure. On the other hand, the RS structure is a metastable phase which may exist if temperature and load histories are carefully controlled. In contrast, it is not possible for HX to exist without loading since no energy well is seen for it on the energy surface. Of course, the enthalpy surface can be modified by appropriate external loading to include a local minimum (well) at the HX structure. Tensile loading of sufficient magnitude along the *b*-direction is such an example and has been shown to cause the WZ → HX phase transformation [6]. Crystallographically, the two-way WZ ↔ HX transformation occurs through smooth lattice structure evolution without the formation of defects or intermediate structures. In particular, the process can be illustrated by a look at the buckling and unbuckling of the [0001] Zn and O basal planes.

Figure 12 shows the evolution of the 3-D O–Zn–O bond angle (α) at various stages of deformation. The strain values are associated with the loading process of
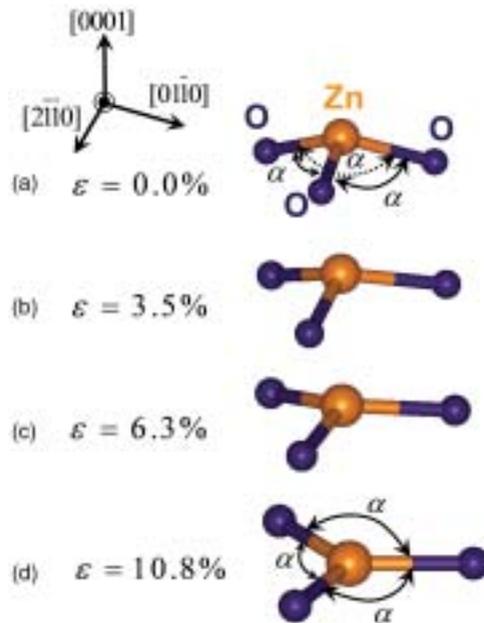
Figure 12.   Increase in the O–Zn–O bond angle (α) between Zn and O atoms on [0001] basal planes at various levels of strain during tensile loading along the [01$\bar{1}$0] wire axis.

the 40.81×39.89 Å^2 wire. The evolution of α during unloading is very similar except that the corresponding wire strain values are slightly different. For a perfect, undeformed WZ lattice, $\alpha \approx 108.2°$ (figure 12a). As deformation progresses, α increases as loading is increased and the structure evolves (figures 12b and c). Upon full WZ $\rightarrow$ HX transformation, the basal planes flatten out and α becomes 120° (figure 12d), at the same time, a new bond is formed along the [0001] axis (figures 4b and c). During unloading, the reverse process is seen, with α decreasing as the load is decreased. The lack of defect or intermediate structure formation in the process makes ZnO nanowires different from FCC metal nanowires such that the energy requirement for the nucleation of the WZ $\leftrightarrow$ HX transformation is very low. Therefore, during the actual unloading of a HX wire, the barrier for the HX $\rightarrow$ WZ transformation is primarily due to the breaking of the additional [0001] bond formed during the forward transformation. This barrier is relatively small [6] and is easily overcome by the strain energy stored in the HX structure. Consequently, spontaneous HZ $\rightarrow$ WZ transformation occurs at all temperatures and no SME is observed in the ZnO nanowires.

4. Conclusions

A novel pseudoelastic behaviour we discovered recently in [01$\bar{1}$0]-oriented ZnO nanowires over the temperature range 100–700 K has been characterized.

MD simulations of the uniaxial tensile loading and unloading of nanowires with lateral dimensions between 18 and 41 Å show that this behaviour results from a unique structural transformation from WZ to a previously unknown phase (herein referred to as HX). Crystallographically, this newly discovered polymorph of ZnO has a five-fold coordination, in contrast to the four-fold coordination of the initial WZ structure, implying that the transformation proceeds towards higher ionicity. The transformation is fully reversible upon unloading with recoverable strains up to 16%. The hysteretic dissipation associated with a loading-unloading cycle is 0.05–$0.14 \, \text{GJ m}^{-3}$ and this value is significantly lower then the value for the reversible WZ–RS transformation in ZnO.

Significant temperature and size dependence of the pseudoelastic response is observed. In particular, the critical stress for the nucleation of the HX phase and the maximum recoverable strain decreases as temperature increases. In addition, the critical stress is lower at smaller wire sizes. Extensive surface reconstructions that minimize surface charge polarity and surface energy contribute to these temperature- and size-effects.

Unlike the pseudoelasticity in fcc metal nanowires, which was discovered recently by Liang *et al.* [2–4] and underlies a novel shape memory effect, the pseudoelasticity in the ZnO nanowires analyzed here does not lead to a SME. The primary reason for this lack of an SME is the absence of an energy barrier between the WZ and the HX lattice structures when no external loading is applied. The absence of an energy barrier between WZ and HX at zero stress can be regarded as a consequence of the smooth and continuous nature of the crystallographic transition which does not require the formation of defects such as dislocations and twin boundaries. The result is that stretched HX ZnO nanowires can spontaneously revert back to the WZ state at any temperature.

Acknowledgements

References

[1] K. Otsuka and C.M. Wayman, *Shape Memory Materials* (Cambridge University Press, New York, 1998).
[2] W. Liang and M. Zhou, J. Engng Mater. Technol. **127** 123 (2005).
[3] W. Liang and M. Zhou, Phys. Rev. B **73** 115409 (2006).

[4] W. Liang, M. Zhou and F.J. Ke, Nano Lett. **5** 2039 (2005).
[5] H.S. Park, K. Gall and J.A. Zimmerman, Phys. Rev. Lett. **95** 255504 (2005).
[6] A.J. Kulkarni, M. Zhou, K. Sarasamak, *et al.*, Phys. Rev. Lett. **97** 105502 (2006).
[7] D.J. Binks and R.W. Grimes, J. Amer. Ceram. Soc. **76** 2370 (1993).
[8] D. Wolf, P. Keblinski, S.R. Phillpot, *et al.*, J. Chem. Phys. **110** 8254 (1999).
[9] Z.L. Wang, J. Phys. Cond. Matt. **16** R829 (2004).
[10] Z.L. Wang, Mater. Today **7** 26 (2004).
[11] Z.L. Wang, Annu. Rev. Phys. Chem. **55** 159 (2004).
[12] A.J. Kulkarni, M. Zhou and F.J. Ke, Nanotechnology **16** 2749 (2005).
[13] A.J. Kulkarni and M. Zhou, Acta Mech. Sin. **22** 217 (2006).
[14] A.J. Kulkarni and M. Zhou, Appl. Phys. Lett. **88** 141921 (2006).
[15] J. Diao, K. Gall and M.L. Dunn, Nature Mater. **2** 656 (2003).
[16] J. Diao, K. Gall and M.L. Dunn, Phys. Rev. B **70** 075413 (2004).
[17] J.M. Haile, *Molecular Dynamics Simulation* (Wiley-Interscience, New York, 1997).
[18] S. Melchionna, G. Ciccotti and B.L. Holian, Molec. Phys. **78** 533 (1993).
[19] D. Spearot, K. Jacob and D.M. McDowell, Acta Mater. **53** 3579 (2005).
[20] M. Zhou, Proc. R. Soc. **459** 2347 (2003).
[21] J.M.J.V. Leeuwen, J. Groeneveld and J.D. Boer, Physica **25** 792 (1959).
[22] G.B. Olson and M. Cohen, J. Phys., Paris **43** 4 (1982).
[23] S. Limpijumnong and S. Jungthawan, Phys. Rev. B **70** 054104 (2004).
[24] S. Limpijumnong and W.R.L. Lambrecht, Phys. Rev. Lett. **86** 91 (2001).
[25] F. Claeyssens, C.L. Freeman, N.L. Allan, *et al.*, J. Mater. Chem. **15** 139 (2005).
[26] C.L. Freeman, F. Claeyssens, N.L. Allan, *et al.*, Phys. Rev. Lett. **96** 066102 (2006).
[27] J. Goniakowski, C. Noguera and L. Giordano, Phys. Rev. Lett. **93** 215702 (2004).
[28] R.B. Capaz, H. Lim and J.D. Joannopoulos, Phys. Rev. B **51** 17755 (1995).
[29] D.J. Binks, Computational modelling of zinc oxide and related oxide ceramics. PhD thesis, University of Surrey (1994).
[30] S. Desgreniers, Phys. Rev. B **58** 14102 (1998).
[31] W. Smith and T.R. Forester, *DL_POLY – a Molecular Simulation Routine* (Central Laboratory of Research Councils, Daresbury, 1996).
[32] W. Humphrey and A. Dalke, J. Molec. Graphics **14** 33 (1996).